Journal Name

ARTICLE TYPE

Cite this: DOI: 10.1039/xxxxxxxxxx

Renormalized thermoelectric figure of merit in band-convergent Sb_2Te_2Se monolayer: full electron-phonon interactions and selection rules

Ying Chen,[a,*], Yu Wu,[a,*] Bowen Hou,[a] Jiang Cao,[b] Hezhu Shao,[c] Yiming Zhang,[a] Haodong Mei,[a] Zhilai Fang,[a,†] Heyuan Zhu[a,‡] and Hao Zhang[a,d,§]

Received Date
Accepted Date

DOI: 10.1039/xxxxxxxxxx

www.rsc.org/journalname

The band-convergent strategy by improving density of states effective masses has been proposed and successfully used in past decades to optimize thermoelectric performance in materials or discover new thermoelectric materials. Unfortunately, when performing the band-convergent strategy in materials with multi-peaks (valleys) bandstructures, the effects of interpeak (intervalley) scatterings and couplings between carriers and phonons other than longitudinal acoustic phonon mode are generally neglected in thermoelectric community. Here, based on the *ab-initio* calculations, we investigate in detail the full electron-phonon couplings in Sb_2Te_2Se monolayer with degenerate valence-band peaks, and their influences on electronic transport and thermoelectric properties. We find that, the optical phonon modes dominate the intravalley scatterings for non-degenerate conduction-band electrons, and interpeak scatterings dominate the electron-phonon scatterings for degenerate valence-band holes. The widely-used deformation potential approximation method severely misestimates carrier mobilities in band-convergent systems such as Sb_2Te_2Se monolayer. According to the group-theory argument, the selection rules for the full electron-phonon interactions are derived. Finally, we calculate the momentum and energy-dependent relaxation times considering the full electron-phonon couplings, and the thermoelectric figure-of-merit values at 300/500/700 K are then accurately predicted to be 1.28/2.28/2.98 for p-type doping and 1.86/2.99/3.75 for n-type doping, respectively, which manifests Sb_2Te_2Se monolayer promising for both p- and n-type thermoelectric applications.

1 Introduction

The thermoelectric conversion devices, which convert waste heat into useful electricity, have received widespread attention as an environmentally friendly solution to the global energy crisis[1,2]. The energy-conversion efficiency of thermoelectric (TE) devices is predominantly determined by the TE performance of materials, which is measured by the dimensionless TE figure of merit (zT) defined as $zT = S^2\sigma T/(\kappa_l + \kappa_{el})$, where S is the Seebeck coefficient, σ is the electronic conductivity, T is the absolute temperature, and κ_l/κ_{el} are the lattice/electronic thermal conductivity[3,4]. The quantity of $S^2\sigma$ is usually called as the power factor (PF) related to the electronic transport properties, and the total thermal conductivity κ ($\kappa = \kappa_l + \kappa_{el}$) is the key parameter to characterize the thermal transport properties. In general, high-performance TE materials possess good electronic transport properties (high PF) and poor thermal transport properties (small κ). However, the three parameters of S, σ, and κ_{el} are strongly coupled to each other, e.g. as the carrier concentration increases, the σ increases, accompanied by a decrease in S and an increase in κ_{el}, which makes optimization of zT a challenging task. In past decades, several optimization strategies such as the band convergence[5,6], resonant electronic states[7] and nanostructuring[8], have been proposed to enhance the TE performance in traditional materials or discover new TE materials.

For simple semiconductors in which the single-band simplication model is effective, the power factor PF depends on the den-

[a] School of Information Science and Technology, Fudan University, Shanghai, 200433, China
[b] School of Electronic and Optical Engineering, Nanjing University of Science and Technology, Nanjing 210094, China
[c] Institute of Micro-nano Structures & Optoelectronics, Wenzhou University, Wenzhou 325035, China
[d] Nanjing University, National Laboratory of Solid State Microstructure, Nanjing 210093, China
*These authors contributed equally.
§E-mail: zhangh@fudan.edu.cn
†E-mail: zlfang@fudan.edu.cn
‡E-mail: hyzhu@fudan.edu.cn

sity of states (DOS) effective mass m^*_{DOS} and the mobility μ, i.e. $PF = S^2\sigma \propto \mu m^{*3/2}_{DOS}$. m^*_{DOS} is proportional to the change rate of DOS near the Fermi surface, and related to both band degeneracy N_v and band effective mass m^*_b through $m^*_{DOS} = N_v m^*_b$. In semiconductors, the mobility μ is inversely proportional to the band effective mass m^*_b, meaning that large m^*_b always results in small μ. Therefore, to enhance PF, the so-called band convergence strategy is proposed, which modulates the band structure to realize a large number of degeneracy N_v by degenerate multi-valleys in conduction bands (CBs) or degenerate multi-peaks in valence bands (VBs)[5]. For example, by tuning the compounds ratio in the $PbTe_{1-x}Se_x$ system, the degeneracy N_v of L and Σ valence bands at high temperature can be enlarged to 16, which finally enhances the zT value of the system at 800 K up to 1.8[9]. High TE performance of some traditional TE materials such as $Mg_2Si_{1-x}Sn_x$ solid solution[10] and half-Heusler[11] also benefit from the large band degeneracy N_v due to the high crystal symmetry. In the originally proposed band-convergence strategy, high band convergence is beneficial for the enhancement of m^*_{DOS} without influencing other parameters, leading to the enhancement of PF. However, the strong intervalley scatterings for CB electrons or VB holes resulted from the band convergence are totally neglected, which may deteriorate carrier mobilities and Seebeck coefficients, probably fail the band-convergent strategy to enhance PF in some TE materials[12]. Therefore, thorough investigations on the influence of full electron-phonon (*el-ph*) couplings on the electronic transport properties are indispensable to accurately predict thermoelectric performance of materials.

Antimony telluride (Sb_2Te_3) and related metal chalcogenide semiconductors (Bi_2Te_3 and etc.) are well known for the successfully commercial applications in TE devices working at low temperature for decades. Inspired by the optimization strategies such as quantum confinement effects and electronic resonance states, a series of Sb_2Te_3-based TE materials including Sb_2Te_3 thin films[13,14], $Sb_2Te_{3-x}Se_x$ solid solutions[15,16], and Bi_2Te_3/Sb_2Te_3 superlattices[17,18] have been experimentally fabricated and investigated, and the zT values of these materials are much larger than that in bulk Sb_2Te_3[19]. Recently, new Sb_2Te_2Se monolayer formed by replacing the Te atoms in the middle layer of Sb_2Te_3 monolayer by Se atoms was reported[20], in which high carrier mobility, small band effective mass and multi-peaks in VBs are observed. Diznab[21] et al. showed that three of the four possible valleys in Sb_2Te_2Se monolayer are well aligned, resulting in a large band degeneracy N_v of 18 and making it promising for future microelectronic and TE applications.

In this work, based on Wannier interpolation and density functional perturbation theory (DFPT), the full *el-ph* coupling matrix elements are calculated by using the EPW packages[22,23], and the full mode- and momentum-resolved *el-ph* interactions for CB electrons and VB holes are systematically investigated. To survey the impact of interpeak scattering and intrapeak (intravalley) scatterings on the holes (electrons) transport properties, we calculate the carriers mobilities based on the full *el-ph* interactions and deformation potential approximation (DPA) method, respectively. For the thermal transport properties, the temperature-dependent lattice thermal conductivities and other related thermal properties of the Sb_2Te_2Se monolayer at natural isotopic concentration are investigated in detail as well. Finally, using the energy- and momentum-dependent relaxation times considering the full *el-ph* couplings and constant relaxation times obtained from DPA method, we predict accurately the zT values and related thermoelectric properties, respectively. Our results manifest the necessity of full *el-ph* interactions researches and the potential of Sb_2Te_2Se to be a candidate in TE devices.

2 Computational details

Based on the density functional theory (DFT), the electronic band structure is calculated by the Vienna *ab initio* simulation package (VASP), in which Perdew-Burke-Ernzerhof (PBE) exchange correlation functional of the generalized gradient approximate (GGA) and the projector-augmented-wave (PAW) pseudopotential are used. The **k**-mesh in the process of conducting the self-consistent calcualtion of electronic system is set to be 21×21×1. The plane wave cutoff kinetic energy is set to 600 eV, the convergence thresholds are set to -10^{-3} eV/Å for Hellman-Feynman (HF) force convergence and 10^{-5} eV for electronic energy differences convergence.

We also carry out DFT using the QUANTUM ESPRESSO code[24] with the PBE exchange correlation functional[25], and the norm-conserving pseudopotentials (NCPP) method with a kinetic energy cutoff of 90 Ry used to perform the ground-state calculations of charge density and band structure. A vacuum space of 20 Å is set along the perpendicular direction to eliminate the spurious interlayer interacions due to the periodic boundary conditions. For the lattice dynamical properties, the coarse Monkhorst-Pack **k**- and **q**-mesh for the material are taken as 12×12×2 and 6×6×2 respectively. The Wannier interpolation method is used to generate the ultradense fine grid to describe the processes of *el-ph* scattering accurately, implemented in the Wannier90[26] and EPW codes[22,23]. Accordingly, much finer **k** and **q** meshes of 120×120×2 and 48×48×2 respectively are used to calculate the *el-ph* coupling matrix to guarantee the numerical convergence.

Based on the Boltzmann transport theory, the electron mobility can be defined as[27],

$$\mu_{\alpha\beta} = \frac{-e}{n_e \Omega} \sum_{n\in CB} \int \frac{d\mathbf{k}}{\Omega_{BZ}} \frac{\partial f^0_{n\mathbf{k}}}{\partial \varepsilon_{n\mathbf{k}}} u_{n\mathbf{k},\alpha} u_{n\mathbf{k},\beta} \tau^e_{n\mathbf{k}} \tag{1}$$

where n_e is the number of electrons in the unit cell, Ω and Ω_{BZ} denote the volumn of the unit cell and the first Brillouin zone, respectively, $f^0_{n\mathbf{k}}$ is the Fermi-Dirac distribution, $u_{n\mathbf{k},\alpha} = h^{-1}\partial\varepsilon_{n\mathbf{k}}/\partial k_\alpha$ is the velocity of the single-particle electron with the eigenvalue $\varepsilon_{n\mathbf{k}}$. The full interaction between electron and phonon is described by the parameter $\tau^e_{n\mathbf{k}}$ which is expressed as[27]

$$\frac{1}{\tau^{e}_{n\mathbf{k}}} = 2\mathrm{Im}\Sigma^{el\text{-}ph}_{n\mathbf{k}}(\omega) = \frac{2\pi}{\hbar}\sum_{m\lambda}\int \frac{d\mathbf{q}}{\Omega_{BZ}} |g_{mn\lambda}(\mathbf{k},\mathbf{q})|^2 \times \Big[(1-f^{0}_{m\mathbf{k}+\mathbf{q}}+n_{\mathbf{q}\lambda})\delta(\varepsilon_{n\mathbf{k}}-\varepsilon_{m\mathbf{k}+\mathbf{q}}-\hbar\omega_{\mathbf{q}\lambda}) + (f^{0}_{m\mathbf{k}+\mathbf{q}}+n_{\mathbf{q}\lambda})\delta(\varepsilon_{n\mathbf{k}}-\varepsilon_{m\mathbf{k}+\mathbf{q}}+\hbar\omega_{\mathbf{q}\lambda})\Big] \quad (2)$$

where $\Sigma^{el\text{-}ph}_{n\mathbf{k}}$ is the *el-ph* self-energy for electron $|n\mathbf{k}>$ state and the summation is over all the included band index m for electrons and all the phonon mode with the mode index λ and wavevector $\mathbf{q}$. $\omega_{\mathbf{q}\lambda}$ and $n_{\mathbf{q}\lambda}$ are the frequency and Bose-Einstein distribution of phonons. $\varepsilon_{m\mathbf{k}+\mathbf{q}}$ and $f^{0}_{m\mathbf{k}+\mathbf{q}}$ are the electron eigenvalue and the Fermi-Dirac distribution of the final state with band index m and wavevector $\mathbf{k'}=\mathbf{k}+\mathbf{q}$. The *el-ph* scattering-probability matrix element $g_{mn\lambda}(\mathbf{k},\mathbf{q})$ is defined as[28],

$$g_{mn\lambda}(\mathbf{k},\mathbf{q}) = \left\langle \psi_{m\mathbf{k}+\mathbf{q}} | \Delta_{\mathbf{q}\lambda} V^{KS} | \psi_{n\mathbf{k}} \right\rangle \quad (3)$$

with $\psi_{n\mathbf{k}}$ and $\psi_{m\mathbf{k}+\mathbf{q}}$ being the initial and final electronic Bloch states scattered by phonon $(\lambda,\mathbf{q})$, respectively. $\Delta_{\mathbf{q}\lambda}V^{KS}$ is the variation of the Kohn-Sham potential induced by lattice vibrations.

The in-plane thermal conductivities κ_l of Sb_2Te_2Se monolayer are direction-independent, and can be calculated as the sum of all the phonon modes[29–31],

$$\kappa_l = \kappa_{\alpha\alpha} = \frac{1}{\Omega}\sum_{\lambda} C_\lambda v^2_{\lambda\alpha}\tau^{p}_{\lambda\alpha} \quad (4)$$

where C_λ is the heat capacity of each phonon mode, $v_{\lambda\alpha}$ is the group velocity of mode λ along α direction, and $\tau^{p}_{\lambda\alpha}$ is the relaxation time of mode λ along α direction. The phonon transport properties are calculated by using ShengBTE package, which is based on the full iterative solution of Boltzmann transport equation (BTE) or the relaxation time approximation (RTA) method[32–34]. The q-mesh in the Brillouin zone (BZ) is set as 51×51×1 and the the scale parameter for broadening of Gaussian function is 1.0. The convergence test for q-mesh is shown in Fig. S9. The main inputs for the BTE calculations are the second (harmonic) and third (anharmonic) force constants. Due to the thickness of ~27 Å (including the vacuum layer thickness) used to calculate the thermal transport properties is arbitary in some extent, the lattice thermal conductivities in the 2D units are calculated as well by using the thickness of 3.35 Å (typical thickness for graphene), which are independent of the arbitrarily-defined monolayer thickness.

The harmonic force constants are obtained by solving the Hessian matrix using the Phonopy package based on the density-functional perturbation theory (DFPT) method, in which a 6×6×1 supercell is used. We use the finite difference supercell method to calculate the anharmonic force constant[32], and the 6×6×1 supercells are used. The interactions within the tenth nearest-neighbor atoms for Sb_2Te_2Te monolayer are included. The first-principle calculations here are performed by using the the state-of-art VASP package, and the local density approximation (LDA) potential in the projector-augmented-wave (PAW) pseudo-potential is used. The convergence threshold is set to 10^{-8} eV/Å and the k-mesh in BZ is set as 1×1×1.

Based on the semi-classical BTE and the rigid-band approximation[35], the thermoelectric transport properties are calculated by the BoltzTrap2 package. The temperature- and doping-dependent holes/electrons concentration $c_{h/e}$, electronic conductivity σ, electronic thermal conductivity κ_{el} and Seebeck coefficient S are calculated by[35–37],

$$c_{\mathrm{h}}(T,E_f) = \frac{2}{\Omega}\iint_{\mathrm{BZ}}\left[1-f_0\left(T,\varepsilon,E_f\right)\right]D(\varepsilon)\mathrm{d}\varepsilon \quad (5)$$

$$c_{\mathrm{e}}(T,E_f) = \frac{2}{\Omega}\iint_{\mathrm{BZ}} f_0\left(T,\varepsilon,E_f\right)D(\varepsilon)\mathrm{d}\varepsilon. \quad (6)$$

$$\sigma_{\alpha\beta}(T,E_f) = \frac{1}{\Omega}\int \overline{\sigma}_{\alpha\beta}(\varepsilon)\left[-\frac{\partial f_0(T,\varepsilon,E_f)}{\partial\varepsilon}\right]d\varepsilon, \quad (7)$$

$$\kappa^{el}_{\alpha\beta}(T,E_f) = \frac{1}{e^2T\Omega}\int \overline{\sigma}_{\alpha\beta}(\varepsilon)(\varepsilon-E_f)^2\left[-\frac{\partial f_0(T,\varepsilon,E_f)}{\partial\varepsilon}\right]d\varepsilon, \quad (8)$$

$$S_{\alpha\beta}(T,E_f) = \frac{1}{eT\Omega\sigma_{\alpha\beta}(T,E_f)}\int \overline{\sigma}_{\alpha\beta}(\varepsilon)(\varepsilon-E_f)\left[-\frac{\partial f_0(T,\varepsilon,E_f)}{\partial\varepsilon}\right]d\varepsilon, \quad (9)$$

where f_0 is the Fermi-Dirac distribution, E_f is the chemical potential, $D(\varepsilon)$ is the density of states, $\overline{\sigma}_{\alpha\beta}(\varepsilon)$ is the energy dependent conductivity tensor, which can be obtained by $\overline{\sigma}_{\alpha\beta}(\varepsilon) = \frac{1}{N}\sum_{i,\mathbf{k}}\overline{\sigma}_{\alpha\beta}(i,\mathbf{k})\frac{\delta(\varepsilon-\varepsilon_{i,k})}{d\varepsilon}$, in which N is the number of sampled $\mathbf{k}$ points and $\overline{\sigma}_{\alpha\beta}(i,\mathbf{k})$ can be calculated by the formula based on the kinetic theory, i.e. $\overline{\sigma}_{\alpha\beta}(i,\mathbf{k}) = e^2\tau_{i,\mathbf{k}}u_\alpha(i,\mathbf{k})u_\beta(i,\mathbf{k})$. The velocity of carrier $u_{\alpha,\beta}(i,\mathbf{k})$ is defined by $u_t(i,\mathbf{k}) = \frac{1}{\hbar}\frac{\partial\varepsilon_{i,\mathbf{k}}}{\partial k_t(t=\alpha,\beta)}$. The electron-phonon relaxation time defined by Eq. (2) is treated as both energy-, momentum- and direction-dependent.

3 Results and discussion

3.1 Electronic and phononic bandstructures

Based on the DFT method implemented in VASP, the electronic bandstructure for Sb_2Te_2Se monolayer is calculated and shown in Fig. 1(a) and Fig. S1. The Sb_2Te_2Se monolayer with the space group of $p\bar{3}m1$ as show in Fig. S3, is an indirect-band-gap semiconductor with the bandgap of 0.63 eV, and the conduction-band minimum (CBM) is located at the Γ point while the valence-band maximum (VBM) is located along Γ-K. The VB possesses four local band-maximum of (V_2-V_5) besides the global VBM (V_1), with energy differences of E_{V_2} = 125 meV, E_{V_3} = 331 meV, E_{V_4} = 16.2 meV and E_{V_5} = 15.0 meV lower than the VBM (V_1). The multiple peaks near the Fermi level enhance the DOS effective mass m^*_{DOS} by a factor of the band degeneracy N_v=18, considering the local band-maximum of V_4 (with N_v=6) and V_5 (with N_v=6) with energy difference of $< 2k_BT$ lower than the VBM (V_1, with N_v=6)[6,9]. As shown in Fig. S2, in addition to the reduction of band gap of 0.19 eV, the spin-orbit coupling (SOC) effect is expected to be trivial in the energy range we are considering and will not be included in our following calculations. The trivial effect of SOC is due to the spin degeneracy resulted from the inversion symmetry and time-reverse symmetry of Sb_2Te_2Se monolayer.[20]

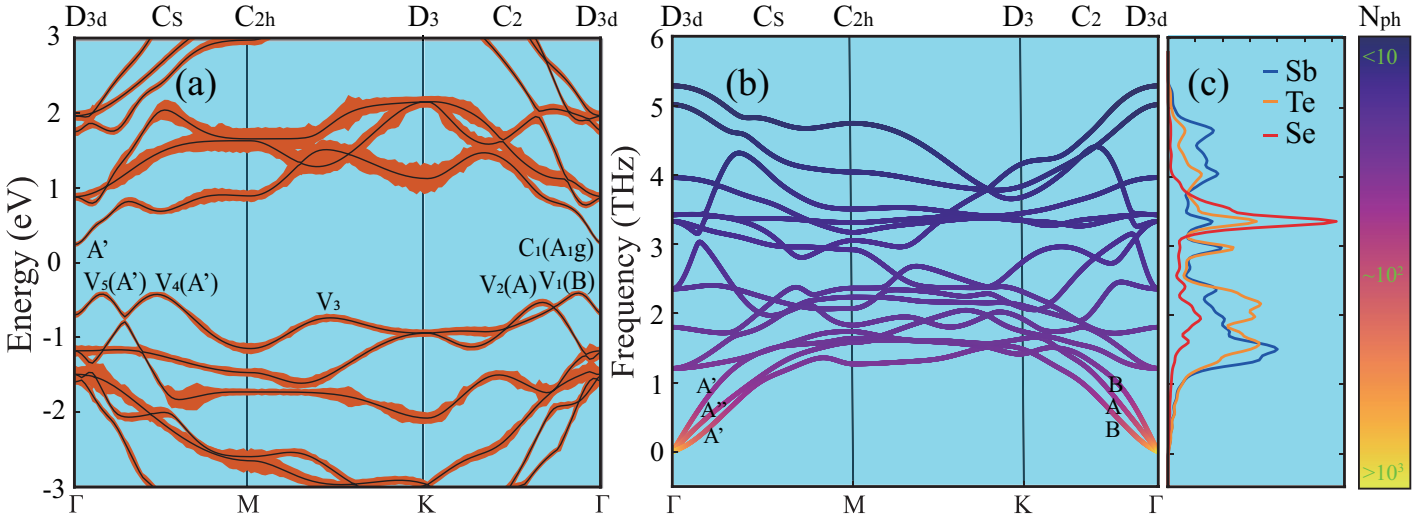

Fig. 1 (a) The electronic bandstructure with the respective total *el-ph* scattering rates along the high symmetry line in the first Brillouin Zone, (b) phonon dispersions with the color representing the average phonon occupancy at 300 K, and (c) phonon partial density of states (PDOS) for Sb_2Te_2Se monolayer.

The calculated phonon dispersion for Sb_2Te_2Se monolayer is shown in Fig. 1(b), in which the color denotes the average phonon occupancy determined by the Bose-Einstein distribution $1/(e^{\hbar\omega/k_BT}-1)$, with $\hbar$ the reduced Planck Constant, k_B the Boltzmann constant, ω the phonon frequency and T the temperature supposed to be 300 K here. The longitudinal acoustic (LA) and transverse acoustic (TA) branches are linear near Γ point, and the out-of-plane acoustic phonon (ZA) branch is quadratic near Γ point due to the rotational invariance and Born-Huang equilibrium conditions[38,39]. At 300 K, the phonon occupation number is larger than unity indicating the existence of phonons at any energy level. The phonon partial density of states (PDOS) shown in Fig. 1(c) indicates that the acoustic branches are contributed by Sb and Te atoms, and the lighter-mass Se atoms contribute dominantly to the PDOS in the range of 3.1∼3.4 THz. The localized phonon vibrations with frequencies of 3.1∼3.4 THz increase the scattering channels for optical phonons, which suppresses the lattice thermal conductivity κ_l as discussed below.

3.2 Electronic transport properties considering full *el-ph* couplings and selection rules

Currently, the thermoelectric transport properties are generally obtained by solving the semi-classical Boltzmann transport equation (BTE) for carriers, within the constant relaxation time approximation (CRTA) and DPA methods. This method, has been widely applied to calculate the zT values for SnSe[40], Bi_2Te_3-[41], Sb_2Te_3-based derivative materials[20], and so on in the thermoelectric community. Especially, the CRTA method has been used to estimate the TE performence of Sb_2Te_2Se monolayer we consider herein, using the constant relaxation time derived from DPA method[42] or reported results[21], which give the zT values of Sb_2Te_2Se monolayer ∼1.0[42] or 0.22/0.46[21]. But the DPA treatment proposed by Bardeen and Shockley[43] only considers the *el-ph* scattering effect via LA phonons on the electrons (holes) at CBM (VBM) in the long-wavelength limit, and totally neglects the effects of intrapeak (intravalley) scattering via phonons other than LA phonons and interpeak (intervalley) scatterings. Therefore, the electronic transport properties and TE performance may be misestimated, especially for band-convergent systems like Sb_2Te_2Se monolayer we consider in this paper.

For comparison, we calculate the effective masses, elastic modulus and deformation potential constants, and further obtain the carrier mobilities and scattering rates based on the DPA method as shown in Table S1, in which a and b directions are defined in Fig. S3. The detailed description of the DPA method can be found elsewhere[44–46]. The calculated electron and hole mobilities at 300 K along a/b directions are 1140/1216 cm^2/Vs and 638/188 cm^2/Vs respectively, which are direction-dependent. However, as shown in Fig. 1(a), the calculated band-resolved *el-ph* scattering rates along the high symmetry line of $\Gamma-M-K-\Gamma$ manifest complex scattering behavior of carriers, especially at high-level dopings. Thus, detailed investigations on full *el-ph* couplings for carriers are required for accurate predictions.

The mode- and energy-resolved *el-ph* scattering rates at 300 K within ∼ 0.4 eV above the CBM for electrons are calculated and shown in Fig. 2(a). The scattering rates calculated based on the DPA method is denoted by dashed lines therein. Compared with the total scattering rates considering full *el-ph* interactions, the scattering rates based on the DPA method are well overestimated for small doping with the chemical potential lower than 0.015 eV, but underestimated for heavy doping with higher chemical potentials. Thus, our calculations show that the DPA method does not always underestimate the scattering rates due to the neglect of the intravalley scatterings via other phonon modes. Considering only the curvature of the electronic structure at CBM along the two specific directions of a/b, while ignoring the direction-, energy- and momentum-dependence of the *el-ph* couplings leads to the significant overestimation or underestimation for the scattering rates. For the *el-ph* couplings for electrons in Sb_2Te_2Se monolayer shown in Fig. 2(a), the contributions from

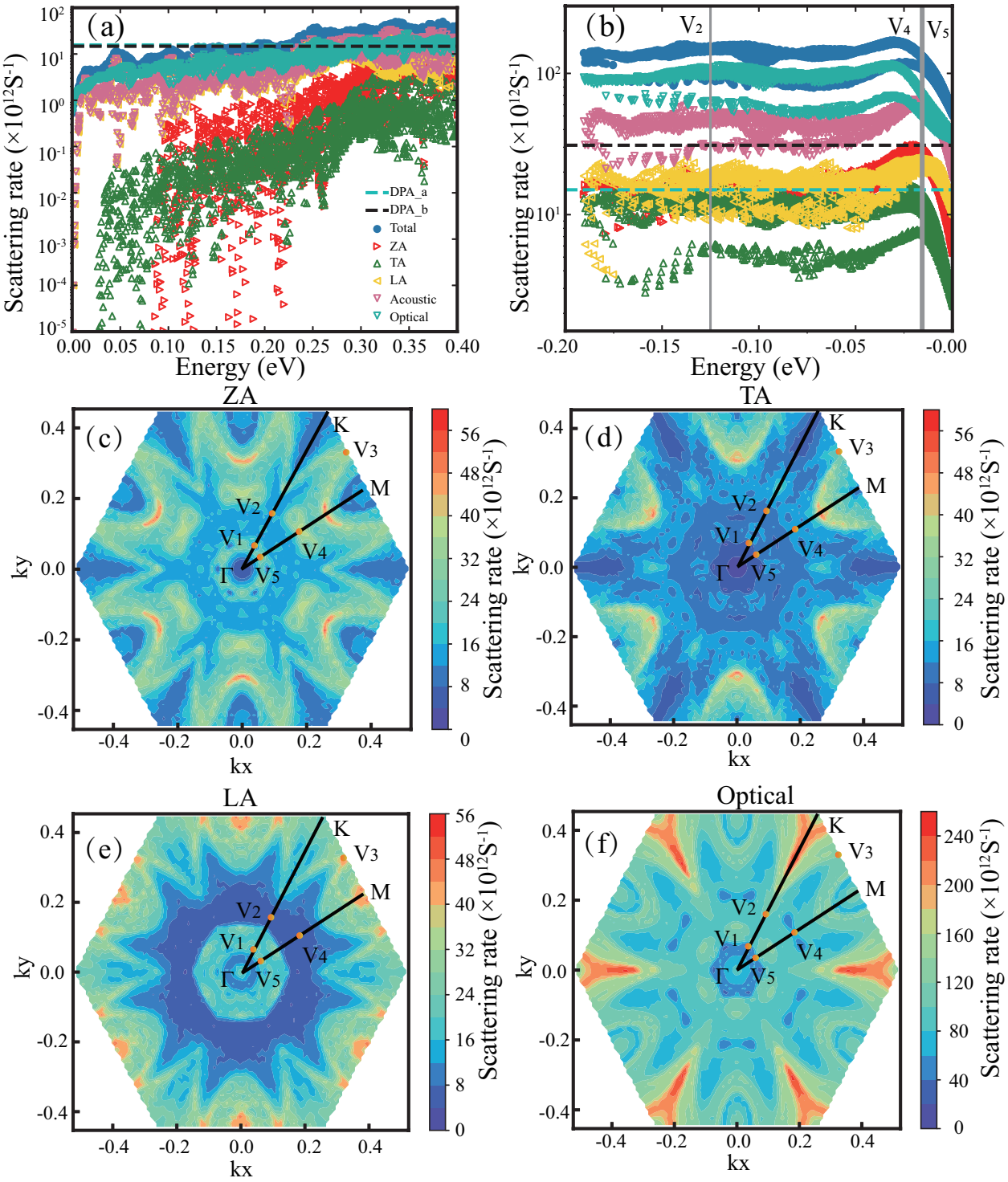

Fig. 2 (a) The scattering rates of electrons in the valley with energies within ~ 0.4 eV from the CBM. (b) The scattering rate of holes in the V_1 peak with energies within ~ 0.2 eV from the VBM. The blue (black) dotted line represents the electron/hole scattering rates along the a (b) direction calculated by the DPA method. (c-f) Mode- and momentum-resolved scattering rates of holes in the highest valence band for Sb_2Te_2Se monolayer.

optical phonon modes are larger than those from acoustic phonon modes, and contributions from LA phonon mode are dominant in the couplings between electrons and acoustic phonons. The intravalley *el-ph* scatterings via the flexural ZA phonon in Sb_2Te_2Se monolayer, which possesses σ_h symmetry, is prohibited according to the Mermin-Wagner theorem[47]. The mode resolved scattering rates for electrons near CBM via the optical phonons are shown in Fig. S4, and the scattering rates for electrons at CBM via each phonon mode are shown in Table S2. The *el-ph* scatterings via most optical phonon modes are negligible, except for O_3, O_5 and O_{12} phonon modes with the respective contributions of 37.8%, 7% and 54.6% to the total scattering rates. As shown in the insets

of Fig. S4(a,d), the vibrations of O_3 and O_{12} phonon modes are out-of-plane and responsible by Se and Te atoms. The mode- and momentum-resolved scattering rates for electrons of the lowest CB shown in Fig. S5 reveals that strong *el-ph* scatterings locate around the M point for TA and LA modes, which probably results from the flat-band effects of the lowest CB around M point as shown in Fig. 1(a).

The calculated full *el-ph* scattering rates for holes within $\sim$ 0.2 eV below the VBM (V_1) are shown in Fig. 2(b), which are quite different from those for electrons. The total *el-ph* scattering rates are significantly larger than results calculated based on the DPA method, although the scattering rates for interactions between holes and acoustic phonon modes are comparable to the DPA results. As shown in Fig. 2(b), due to the nearly degenerate local VBMs of V_4/V_5 and global VBM V_1, the scattering rate increases rapidly with the decrease of chemical potentials in the range of 0.025 eV from VBM, and then remains almost unchanged when the chemical potential decreases further. For the holes near VBM, the scattering rates via optical phonons are larger than those via acoustic phonons, and ZA and LA phonon modes contribute dominantly to the interactions via acoustic phonons. The mode-resolved scattering rates for couplings between holes near VBM and optical phonons are shown in Fig. S6, and the mode-resolved scattering rates for holes at VBM are shown in Table S3. The interpeak scatterings are found to be much stronger than intrapeak scatterings for all phonon modes, contributed 92.5% to the total scattering rates, and the interpeak scatterings via LA, O_9, ZA, O_{10}, O_1 and O_5 phonon modes contribute 15.92%, 12.25%, 11.49%, 9.55%, 7.33% and 6.72% to the total scattering rates for holes at VBM, respectively. The mode- and momentum-resolved scattering rates for holes of the highest VB are shown in Fig. 2(c-f), which reveals the interactions via ZA/LA modes are stronger than those via TA modes, and the large scattering rates between holes and optical phonons along the Γ-K direction is probably due to the flat-band effects as shown in Fig. 1(a). For the *el-ph* interactions between holes and optical phonons, the bifurcation around -0.015 eV can be clearly identified in mode-resolved scattering rates as shown in Fig. 2(b) and Fig. S6.

In order to further understand the underlying mechanism behind the scattering rates and reveal the scattering channels of carriers, based on the group theory, we perform the selection-rules analysis on the *el-ph* interactions in monolayer Sb_2Te_2Se. For simplicity, we only consider the interactions between carriers and acoustic phonons, and similar analysis can be easily performed for the interactions between carriers and optical phonon modes. The formula for the selection rules is expressed in terms of direct product of the irreducible representations (irreps) of the involved phonon mode and the initial state of carriers, which then is decomposed into possible final states of carriers. Thus, it is reasonable to left-multiply the irreps of final states of carriers to simplify the original formula resulted from the orthogonality of irreps, derived as[48],

$$\Gamma^f \otimes \Gamma^{ph} \otimes \Gamma^i = non \quad null \quad (null) \tag{10}$$

Where Γ^{ph} and $\Gamma^{i/f}$ are irreps of involved phonon modes and initial/final carrier states respectively. *null*/*nonnull* indicate the forbidden/allowed scattering channels for carriers scattered by the involved phonon. As shown in Fig 1(a), the CBM of monolayer Sb_2Te_2Se locates at Γ point at the Brillouin zone center, indicating that the initial electron state transforms with A_{1g} irreps, belonging to the little group of D_{3d}. The electron states near CBM transform with A' and A irreps respectively belonging to C_S along Γ – M and C_2 along Γ – K, both of which are the subgroups of D_{3d}. As shown in Fig 1(b), LA and ZA phonon modes transform with A' irreps along Γ – M, and TA modes transform with A irreps along Γ – M. Therefore, restricted by the compatibility relation between different groups and Eq. (10), scattering channels for the CBM electron via both LA and ZA modes along Γ – M direction are allowed, since $A' \otimes A' \otimes A_{1g}$ equals to *nonnull*. The scattering channels for CBM electron via TA phonon modes along Γ – K direction are also allowed, due to *nonnull* of $A \otimes A \otimes A_{1g}$. However, based on the calculated mode-resolved intravalley scattering rates for CBM electrons as shown in Table S2, the scattering channels via TA mode along Γ – K direction and ZA mode along Γ – M direction are forbidden, since the intravalley scattering rate of TA and ZA modes is far smaller than LA mode within CBM of Sb_2Te_2Se. Hence, the only allowed scattering path by symmetry constrain is along Γ – M, dominated by LA phonon mode, which is indicated by green arrow in Fig. 3(a).

The scattering channels for VBM holes in Sb_2Te_2Se monolayer are complex due to the nearly degenerate local VBMs of $V_2 - V_5$ and global VBM of V_1. For simplicity, we only consider the local VBMs of V_4 and V_5, which possess small energy differences of -16.2 and -15.0 meV to V_1, beneficial for the interpeak scatterings of holes. As shown in Fig. 1(a), the irreps of V_1 peak is B belonging to the little group of C_2 along Γ – K, while both peaks of V_4 and V_5 are with irreps of A' belonging to C_S along Γ – M. According to the calculated scattering rates for intra- and inter-peak interactions as shown in Table S3, the contributions of phonon modes in intrapeak scatterings are negligible compared to those of interpeak interactions, indicating the interpeak sactterings predominate the *el-ph* interactions for VBM holes. However, there is no any compatibility relationship between C_2 and C_S group, which forbids the interpeak scatterings between V_1 and V_4 (V_5) along high symmetry lines. In order to resolve such contradiction, it is reasonable to assume the *el-ph* scattering does not occur along high symmetry lines, instead along non-symmetry line in BZ zone. Therefore, the irreps of the initial/final hole states and all acoustic phonon modes are A due to their little group C_1, and the selection rule gives A⊗A⊗A with *nonnull* value. The corresponding scattering channels are allowed and indicated by red lines in Fig. 3(b), where ZA, TA and LA are all involved in the interpeak scattering processes.

Based on the calulated momentum- and energy-resolved relaxation times, the mobilities for electrons and holes in monolayer Sb_2Te_2Se at temperatures ranging from 100 K to 900 K, can be calculated precisely as shown in Fig. 4. The carrier mobility decreases with the increase of the temperature due to stronger *el-ph* interactions at higher temperatures. As mentioned above, the total scatterings rates for CBM electrons calculated by considering full *el-ph* interactions are smaller than those based on the DPA

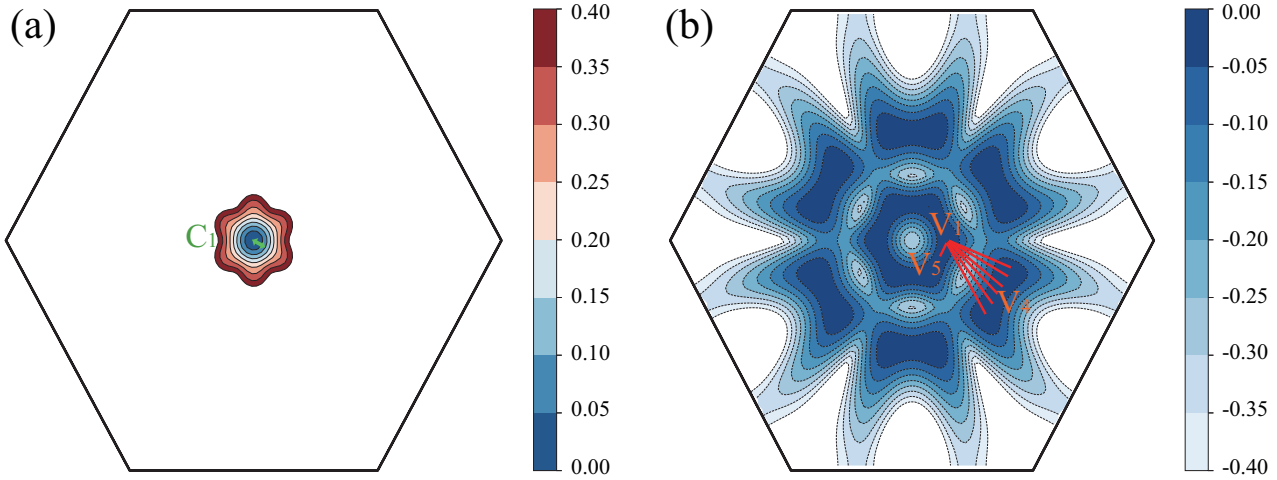

Fig. 3 Scattering channels for inter- and intra- valley (peak) scatterings for (a) CBM electrons and (b) VBM holes of Sb_2Te_2Se. The countour lines of CBM ranges from 0.00 eV to 0.40 eV; and the countour lines of VBM ranges 0.00 eV to -0.40 eV. Green arrow and red lines respectively indicate the scattering channels fro CBM electrons and VBM holes.

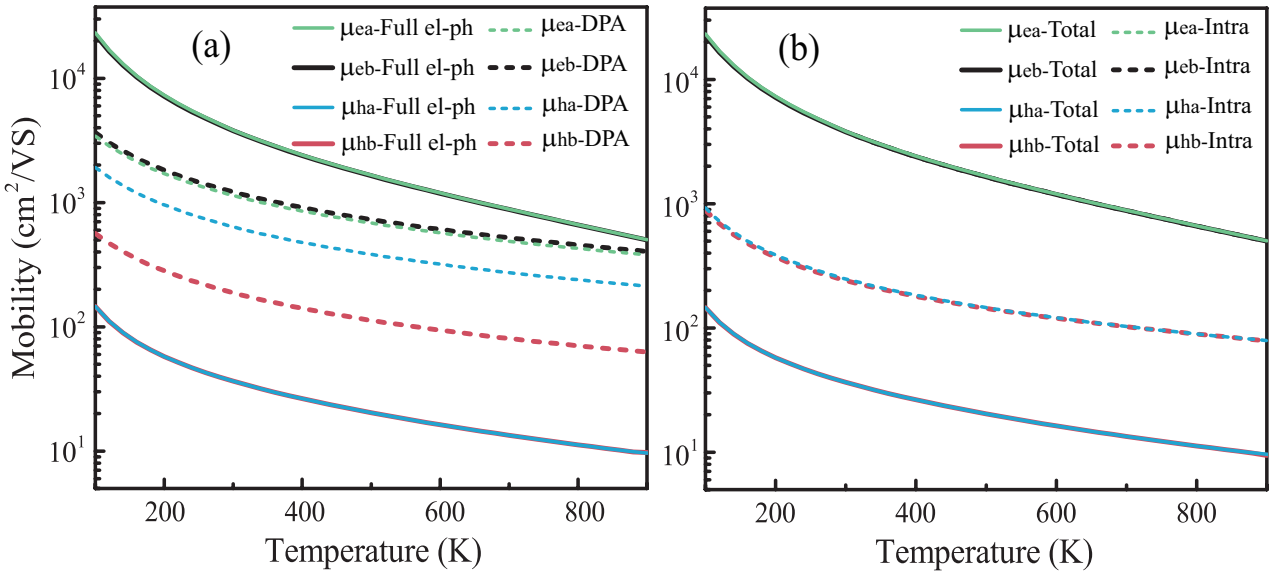

Fig. 4 The comparison of carrier mobilities calculated by (a) DPA method and considering the full *el-ph* couplings, and (b) including the full *el-ph* scatterings and only the intra-valley (peak) scatterings for electrons and holes for Sb_2Te_2Se monolayer at 100∼900K.

method, as shown in Fig. 2(a), while the situation for VBM holes is reverse as shown in Fig. 2(b). Therefore, as shown in Fig. 4(a), the electron mobilities calculated based on the full *el-ph* couplings are larger than those based on the DPA method, while the hole mobilities calculated based on the full *el-ph* couplings are one order in magnitude smaller than the DPA results. Moreover, the DPA calculations obviously overestimate the anisotropy in Sb_2Te_2Se monolayer. By comparing the mobilities calculated by including the full *el-ph* scatterings and only the intravalley (intrapeak) scatterings shown in Fig. 4(b), the electron mobilities in both the *a* and *b* directions are essentially coincident, while the hole mobilities of intrapeak scatterings are much larger than those considering the full *el-ph* scatterings. Thus, the transport properties of holes in Sb_2Te_2Se monolayer are significantly affected by the interpeak scatterings, which is consistent with the aforementioned scattering rates calculations.

3.3 Phonon transport properties

By calculating the 2^{nd}- and 3^{rd}-order interatomic force constants (IFC) and based on the full iterative solution of Boltzmann transport equation (BTE) method, we calculate the lattice thermal conductivity κ_l at temperatures from 100 K ∼ 1000 K and other phonon transport properties including mode-resolved group velocity, relaxation times, Grüneisen parameters and three-phonon phase spaces, which are shown and discussed in detail in Supporting Informations. The isotope scatterings contribute trivially, while the Umklapp process of the anharmonic phonon scatterings and the acoustic phonons contribute significantly to the heat transport process in monolayer Sb_2Te_2Se. To further understand the role of the three-phonon scatterings and contributions from

acoustic phonon modes in the heat conduction process, we also calculate the lattice thermal conductivity κ_l according to the Slack model,

$$\kappa_L = A\frac{\bar{M}\Theta_D^3\delta n^{1/3}}{\gamma^2 T} \tag{11}$$

$$A = \frac{2.43\times10^{-6}}{1-0.514/\gamma+0.228/\gamma^2} \tag{12}$$

where $\bar{M}$ is the averaged atomic mass, δ^3 is the average atomic volume, and γ is the Grüneisen parameter, which is equal to 2.48 at room temperature. Θ_D is the Debye temperature. For temperatures above the Θ_D, all phonon modes are excited and contribute to the lattice thermal conductivity κ_l. From the averaged elastic-wave velocity v_m, the Θ_D can be calculated by[49],

$$\Theta_D = \frac{h}{k_B}\left[\frac{3n}{4\pi}\left(\frac{N_A\rho}{M}\right)\right]^{\frac{1}{3}} v_m \tag{13}$$

where h is the Planck constant, k_B is the Boltzmann constant, n is the number of atoms per unit cell, N_A is Avogadro constant, ρ is the crystal density, M is the molar mass, and v_m can be calculated by,

$$v_m = \left[\frac{1}{3}\left(\frac{2}{{v_T}^3}+\frac{1}{{v_L}^3}\right)\right]^{-\frac{1}{3}} \tag{14}$$

where v_T/v_L is the transverse/longitudinal sound velocity, and can be calculated by bulk modulus B and shear modulus G from Navier's equation,

$$v_T = \left(\frac{G}{\rho}\right)^{\frac{1}{2}} \tag{15}$$

$$v_L = \left(\frac{B+\frac{4G}{3}}{\rho}\right)^{\frac{1}{2}} \tag{16}$$

where the bulk and shear moduli of B/G are the average of the B_V/G_V calculated by the Voigt approximation and the B_R/G_R calculated by the Reuss approximation[50]. The calculated B, G and Θ_D are 5.268 J/m^2, 3.817 J/m^2, 76.794 K, respectively, and the Θ_D is significantly lower than bulk Sb_2Te_3 (160 K[51]) and Bi_2Te_3 (155 K[51]). Thus, due to the dimensionality-reduction effects and the interface scatterings, the Θ_D of two-dimensional materials are lower in Bi_2Se_3/Bi_2Te_3-based chemical compounds, which further leads to the lower lattice thermal conductivities compared to the bulk counterparts. The κ_l at 300K calculated by Eq. (11) is 0.62 W/mK, which is smaller than that of 1.02 W/mK calculated by iteratively solving the BTE using the ShengBTE software package. The underestimation of κ_l by the Slack model is due to the complete neglect of the contribution from optical phonons to the heat transport process[52], which contribute 23% to κ_L as shown in Fig. S7(b).

3.4 Thermoelectric performance

Using the energy- and momentum-dependent relaxation times considering full *el-ph* couplings and the constant relaxation times obtained from DPA method, the chemical potential dependent thermoelectric performance for Sb_2Te_2Se monolayer is calculated, and the results are shown in Fig. 5. The constant relaxation times are calculated according to $\tau = \mu^{2D}m^*/e$, and the calculated results are listed in Table S1, where the mobilities μ^{2D} are calculated based on the DPA method discussed above. The calculated electronic transport properties including Seebeck coefficient S, electronic conductivity σ and power factor PF are shown in Fig. 5 (a-c), in which the TE properties calculated based on the full *el-ph* couplings are denoted by the solid lines. As we know, the Seebeck coefficient S is related to the logarithmic energy derivatives of DOS D(ε) and the electronic relaxation time $\tau(\varepsilon)$ at the Fermi level E_f according to the well known Mott relation,

$$S = -\frac{\pi^2}{3}\frac{k_B^2 T}{e}\left[\frac{\partial \ln D(\varepsilon)}{\partial\varepsilon}+\frac{\partial \ln \tau_e(\varepsilon)}{\partial\varepsilon}\right]_{E_f} \tag{17}$$

where E_f is the chemical potential. As discussed above, the local maximum V_4 and V_5 in the highest VB in the reduced Brillouin zone lead to a large band degeneracy N_v=18, which results in large Seebeck coefficients S. Due to the increasing carrier concentration c, the S gradually decreases as the temperature increases, and the maximum S for Sb_2Te_2Se monolayer at 300/500/700 K are 998/577/399 μVK^{-1} for p-type doping and -1036/-599/-409 μVK^{-1} for n-type doping, respectively. It is well known that σ is proportional to the carrier concentration and mobility. From the calculated σ shown in Fig. 5(b), when the doping concentration is small ($|E_f| < 0.3$ eV), an increase in temperature would lead to an increase in carrier concentration, which results in an increase in σ, when the doping concentration is larger ($|E_f| > 0.3$ eV), the change of carrier concentration caused by temperature increase is not obvious, and the decrease of carrier mobility leads to the decrease of σ. Thus, the maximum PF ($=S^2\sigma$) values decrease with the increasing temperature. At 300/500/700 K, the maximum PF values of 6.6/5.1/4.0 mWm^{-1}K^{-2} for p-type doping and 10.0/6.3/4.3 mWm^{-1}K^{-2} for n-type doping. By comparing with the results calculated by using the constant relaxation times obtained from the DPA shown by the dotted line in Fig. 5 (a-b), we find that the S is roughly insensitive to the two methods, and the σ calculated by the CRTA is much higher than that calculated considering full *el-ph* interactions especially for p-type doping, which is mainly caused by neglecting the effects of intravalley scatterings other than LA phonons and intervalley scatterings.

The κ_l values at 300/500/700 K are 1.02/0.62/0.44 W/mK, respectively. According to the well-known Wiedemann-Franz law, i.e. $\kappa_{el} = L\sigma T$, where L is the Lorenz number, κ_{el} is proportional to σ. But κ_{el} shown in Fig. 5 (d) is not strictly proportional to σ shown in Fig. 5(b), which is due to the fact that Wiedemann-Franz law only apply to metals at high temperatures rather than Sb_2Te_2Se monolayer considered as semiconductor. In fact, the ratio $\kappa_{el}/\sigma T$ is rather complicate herein[53]. Since κ_l is critical for thermoelectric properties and is inversely proportional to the temperature, the maximum zT value increases with increasing temperature. As shown in Fig. 5 (e), the maximum zT value at 300/500/700 K reach 1.28/2.28/2.98 for p-type doping and 1.86/2.99/3.75 for n-type doping, respectively, which are comparable or larger than many traditional thermoelectric materials

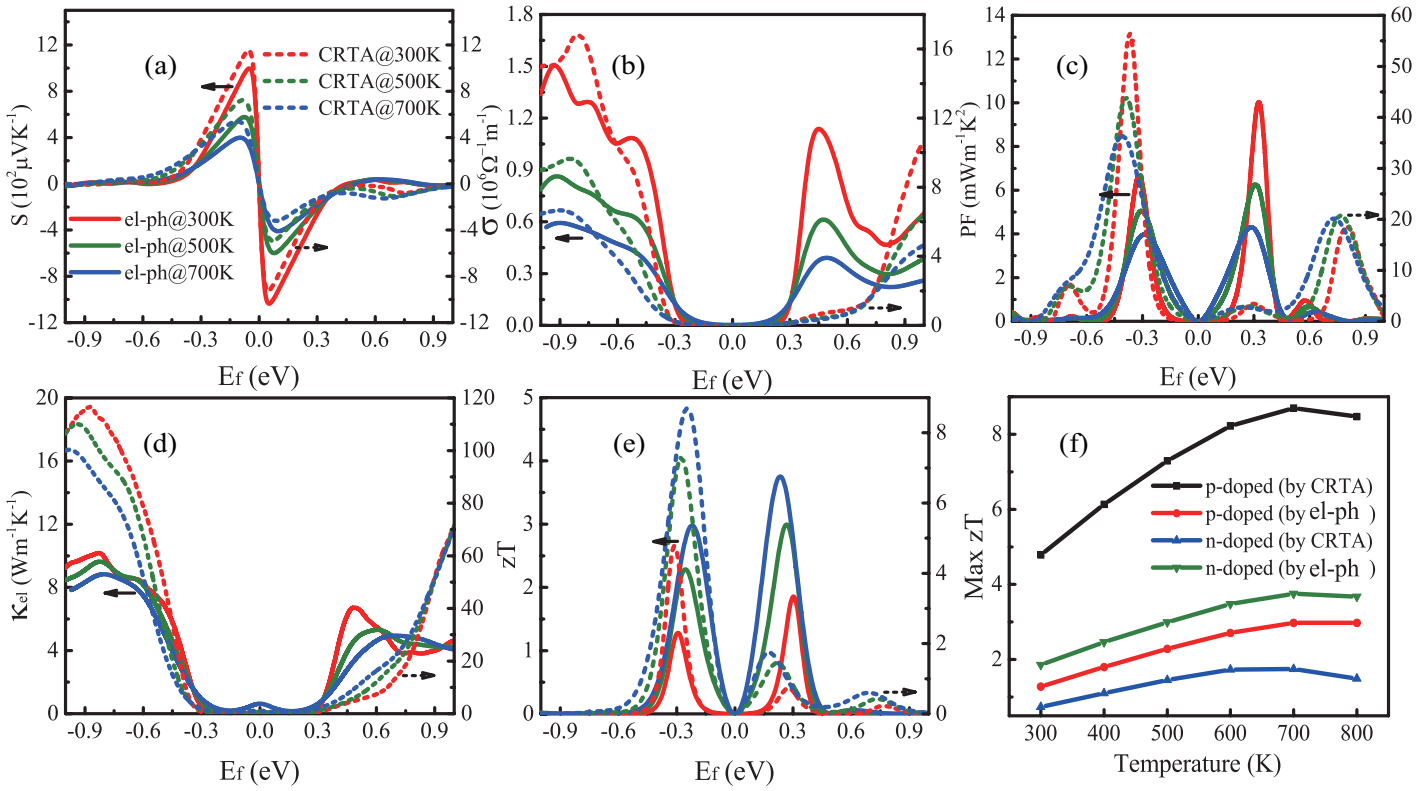

Fig. 5 The comparison of TE performence by CRTA method and using the relaxation considering full *el-ph* couplings. (a) Seebeck coefficients, (b) Electronic conductivities, (c) Power factors, (d) The electronic thermal conductivity and (e) zT values at 300/500/700 K. (f) The maximum zT values at 300∼800 K.

like single-QL Bi_2Te_3 (∼0.77 at 300K)[54], bulk PbTe (∼1.4 at 700 K)[5] and monolayer β-SnSe (∼2.06 at 300 K)[55], indicating that Sb_2Te_2Se monolayer is promising in TE applications, especially for n-type TE devices. The maximum zT values calculated using the energy- and momentum-dependent relaxation times considering full *el-ph* couplings for n-type doping are larger than those for p-type doping, and both of them reach the maximum value at 700 K. Due to the misestimation for electronic transport properties by DPA method as discussed above, the CRTA method overestimates the zT values for p-type doping while underestimates those for n-type doping. In addition, we have compared the TE performance with and without considering VDW interactions, respectively, which reveals that, the change in zT values induced by VDW interactions is less than 4%.

4 Conclusion

We have systematically investigated the *el-ph* couplings in the Sb_2Te_2Se monolayer. The multi-peaks in the highest valence band causes the strong interpeak scatterings, and the hole-optical phonons scatterings dominate the hole scattering process near the VBM. Unlike holes, the scattering processes of electrons near the CBM are dominated by the intravalley scatterings, with O_3 and O_{12} dominating the intravalley scatterings for CBM electrons. The electron and hole mobilities of Sb_2Te_2Se monolayer based on the full $el-ph$ couplings are 3835/3785 cm^2/Vs and 37/37 cm^2/Vs along a/b direction at 300 K, respectively, while the DPA method misestimates the mobilities due to the neglected interpeak scatterings and intrapeak electron-phonon (expect for LA mode) couplings. From the thermal transport properties calculated by iteratively solving the BTE, the anharmonic phonon scatterings are dominated by the Umklapp process and 77% of heat transport is carried by acoustic phonons. The lattice thermal conductivity is very small, which is 1.02 W/mK at room temperature. Using the momentum- and energy-dependent relaxation times considering the full $el-ph$ couplings and the constant relaxation times obtained from DPA method, we have calculated the thermoelectric performence and found that the CRTA method accurately estimates the S and overestimates the σ for p-type doping. The zT values for both p-doping and n-doping are very large, reaching 1.28/2.28/2.98 for p-type doping and 1.86/2.99/3.75 for n-type doping at 300/500/700 K, respectively. Thus, Sb_2Te_2Se monolayer is a promising candidate for future microelectronic and thermoelectric applications.

Acknowledgement

This work is supported by the National Natural Science Foundation of China under Grant Nos. 11374063, 62074039 and 12004074 and Shanghai Municipal Natural Science Foundation under Grant Nos. 19ZR1402900 and 18ZR1402500.

References

1 W. G. Zeier, A. Zevalkink, Z. M. Gibbs, G. Hautier, M. G. Kanatzidis and G. J. Snyder, *Angew. Chem. Int. Ed.*, 2016, **55**, 6826–6841.

2 G. Zheng, X. Su, H. Xie, Y. Shu, T. Liang, X. She, W. Liu, Y. Yan, Q. Zhang, C. Uher, M. G. Kanatzidis and X. Tang, *Energy Environ. Sci.*, 2017, **10**, 2638–2652.

3 X. Liu, D. Wang, H. Wu, J. Wang, Y. Zhang, G. Wang, S. J. Pennycook and L.-D. Zhao, *Adv. Funct. Mater.*, 2019, **29**, 1806558.

4 H.-S. Kim, N. A. Heinz, Z. M. Gibbs, Y. Tang, S. D. Kang and G. J. Snyder, *Mater. Today*, 2017, **20**, 452–459.

5 Y. Pei, H. Wang and G. J. Snyder, *Adv. Mater.*, 2012, **24**, 6125–6135.

6 W. Liu, X. Tan, K. Yin, H. Liu, X. Tang, J. Shi, Q. Zhang and C. Uher, *Phys. Rev. Lett.*, 2012, **108**, 166601.

7 J. W. Simonson, D. Wu, W. J. Xie, T. M. Tritt and S. J. Poon, *Phys. Rev. B*, 2011, **83**, 235211.

8 M. Dresselhaus, G. Chen, M. Tang, R. Yang, H. Lee, D. Wang, Z. Ren, J.-P. Fleurial and P. Gogna, *Adv. Mater.*, 2007, **19**, 1043–1053.

9 Y. Pei, X. Shi, A. LaLonde, H. Wang, L. Chen and G. J. Snyder, *Nature*, 2011, **473**, 66–69.

10 W. Liu, Q. Zhang, X. Tang, H. Li and J. Sharp, *J.Electron.Mater*, 2011, **40**, 1062–1066.

11 W. G. Zeier, J. Schmitt, G. Hautier, U. Aydemir, Z. M. Gibbs, C. Felser and G. J. Snyder, *Nat.Rev.Mater*, 2016, **1**, 1–10.

12 Y. Wu, B. Hou, C. Ma, J. Cao, Y. Chen, Z. Lu, H. Mei, H. Shao, Y. Xu, H. Zhu, Z. Fang, R. Zhang and H. Zhang, *Mater. Horiz.*, 2021, 10.1039/D0MH01802C.

13 P. Wanarattikan, P. Jitthammapirom, R. Sakdanuphab and A. Sakulkalavek, *Advances in Materials Science and Engineering*, 2019, **2019**, 6954918.

14 Z. Li, N. Miao, J. Zhou, Z. Sun, Z. Liu and H. Xu, *Nano Energy*, 2018, **43**, 285–290.

15 D. Das, S. Das, P. Singha, K. Malik, A. K. Deb, A. Bhattacharyya, V. A. Kulbachinskii, R. Basu, S. Dhara, S. Bandyopadhyay and A. Banerjee, *Phys. Rev. B*, 2017, **96**, 064116.

16 D. Das, K. Malik, A. K. Deb, V. A. Kulbachinskii, V. G. Kytin, S. Chatterjee, D. Das, S. Dhara, S. Bandyopadhyay and A. Banerjee, *EPL*, 2016, **113**, 47004.

17 G. Bulman, P. Barletta, J. Lewis, N. Baldasaro, M. Manno, A. Bar-Cohen and B. Yang, *Nat. Commun.*, 2016, **7**, 10302.

18 N. F. Hinsche, B. Y. Yavorsky, M. Gradhand, M. Czerner, M. Winkler, J. Koenig, H. Boettner, I. Mertig and P. Zahn, *Phys. Rev. B*, 2012, **86**, 085323.

19 D. Rowe, *Thermoelectrics Handbook: Macro to Nano*, CRC Press, Boca Raton, 1st edn., 2006.

20 K. Zhao, P. Qiu, X. Shi and L. Chen, *Advanced Functional Materials*, 2019, **n/a**, 1903867.

21 M. R. Diznab, I. Maleki, S. M. V. Allaei, Y. Xia and S. S. Naghavi, *ACS Applied Materials & Interfaces*, 2019, **11**, 46688–46695.

22 J. Noffsinger, F. Giustino, B. D. Malone, C.-H. Park, S. G. Louie and M. L. Cohen, *Computer Physics Communications*, 2010, **181**, 2140–2148.

23 S. Poncé, E. Margine, C. Verdi and F. Giustino, *Comput.Phys.Commun.*, 2016, **209**, 116–133.

24 P. Giannozzi, S. Baroni, N. Bonini, M. Calandra, R. Car, C. Cavazzoni, D. Ceresoli, G. L. Chiarotti, M. Cococcioni, I. Dabo, A. D. Corso, S. de Gironcoli, S. Fabris, G. Fratesi, R. Gebauer, U. Gerstmann, C. Gougoussis, A. Kokalj, M. Lazzeri, L. Martin-Samos, N. Marzari, F. Mauri, R. Mazzarello, S. Paolini, A. Pasquarello, L. Paulatto, C. Sbraccia, S. Scandolo, G. Sclauzero, A. P. Seitsonen, A. Smogunov, P. Umari and R. M. Wentzcovitch, *Journal of Physics: Condensed Matter*, 2009, **21**, 395502.

25 J. Perdew, K. Burke and M. Ernzerhof, *Phys. Rev. Lett.*, 1996, **77**, 3865–3868.

26 A. A. Mostofi, J. R. Yates, G. Pizzi, Y.-S. Lee, I. Souza, D. Vanderbilt and N. Marzari, *Comput. Phys. Commun.*, 2014, **185**, 2309 – 2310.

27 J. Xi, D. Wang, Y. Yi and Z. Shuai, *The Journal of Chemical Physics*, 2014, **141**, 034704.

28 S. Baroni, S. de Gironcoli, A. D. Corso and P. Giannozzi, *Reviews of Modern Physics*, 2001, **73**, 515–562.

29 W. Li, J. Carrete and N. Mingo, *Appl. Phys. Lett.*, 2013, **103**, 253103.

30 T. Ouyang and M. Hu, *Phys. Rev. B*, 2015, **92**, 235204.

31 B. Peng, H. Zhang, W. Chen, B. Hou, Z.-J. Qiu, H. Shao, H. Zhu, B. Monserrat, D. Fu, H. Weng and C. M. Soukoulis, *npj 2D Materials and Applications*, 2020, **4**, 14.

32 W. Li, L. Lindsay, D. A. Broido, D. A. Stewart and N. Mingo, *Phys. Rev. B*, 2012, **86**, 174307.

33 W. Li, N. Mingo, L. Lindsay, D. A. Broido, D. A. Stewart and N. A. Katcho, *Phys. Rev. B*, 2012, **85**, 195436.

34 W. Li, J. Carrete, N. A. Katcho and N. Mingo, *Comput.Phys.Commun.*, 2014, **185**, 1747–1758.

35 G. K. Madsen and D. J. Singh, *Comput. Phys. Commun.*, 2006, **175**, 67–71.

36 J. Yang, H. Li, T. Wu, W. Zhang, L. Chen and J. Yang, *Adv. Funct. Mater.*, 2008, **18**, 2880–2888.

37 A. J. Hong, J. J. Gong, L. Li, Z. B. Yan, Z. F. Ren and J.-M. Liu, *J. Mater. Chem. C*, 2016, **4**, 3281–3289.

38 A. Molina-Sanchez and L. Wirtz, *Phys. Rev. B*, 2011, **84**, 155413.

39 G. Qin, Q.-B. Yan, Z. Qin, S.-Y. Yue, M. Hu and G. Su, *PHYSICAL CHEMISTRY CHEMICAL PHYSICS*, 2015, **17**, 4854–4858.

40 H. Mori, H. Usui, M. Ochi and K. Kuroki, *Phys. Rev. B*, 2017, **96**, 085113.

41 C. Zhou and L. Li, *J.Phys.Chem.Solids*, 2015, **85**, 239–244.

42 B. Xu, Q. Xia, J. Zhang, S. Ma, Y. Wang, Q. Xu, J. Li and Y. Wang, *Comput. Mater. Sci.*, 2020, **177**, 109588.

43 J. Bardeen and W. Shockley, *Phys. Rev.*, 1950, **80**, 72–80.

44 B. Hou, Y. Zhang, H. Zhang, H. Shao, C. Ma, X. Zhang, Y. Chen, K. Xu, G. Ni and H. Zhu, *JOURNAL OF PHYSICAL CHEMISTRY LETTERS*, 2020, **11**, 3116–3128.

45 Y. Wu, K. Xu, C. Ma, Y. Chen, Z. Lu, H. Zhang, Z. Fang and R. Zhang, *Nano Energy*, 2019, **63**, 103870.

46 Y. Wu, C. Ma, Y. Chen, B. Mortazavi, Z. Lu, X. Zhang, K. Xu, H. Zhang, W. Liu, T. Rabczuk, H. Zhu, Z. Fang and R. Zhang, *Materials Today Physics*, 2019, **12**, 100164.

47 Y. Nakamura, T. Zhao, J. Xi, W. Shi, D. Wang and Z. Shuai, *Advanced Electronic Materials*, 2017, **3**, 1700143.
48 L. M. Malard, M. H. D. Guimarães, D. L. Mafra, M. S. C. Mazzoni and A. Jorio, *Phys. Rev. B*, 2009, **79**, 125426.
49 Y. Zhuo, A. M. Tehrani, A. O. Oliynyk, A. C. Duke and J. Brgoch, *Nat. Commun.*, 2018, **9**, 1.
50 R. Hill, *Proceedings of the Physical Society. Section A*, 1952, **65**, 349–354.
51 C. Toher, J. J. Plata, O. Levy, M. de Jong, M. Asta, M. B. Nardelli and S. Curtarolo, *Phys. Rev. B*, 2014, **90**, 174107.
52 G. Slack, *Journal of Physics and Chemistry of Solids*, 1973, **34**, 321–335.
53 *Thermal Conductivity: Theory, Properties, and Applications*, ed. T. M. Tritt, Kluwer Academic / Plenum Publishers, New York, 1st edn., 2004.
54 S. Sharma and U. Schwingenschlogl, *ACS Energy Lett.*, 2016, **1**, 875–879.
55 Z.-Y. Hu, K.-Y. Li, Y. Lu, Y. Huang and X.-H. Shao, *NANOSCALE*, 2017, **9**, 16093–16100.